Article

Reservoir Densification, Pressure Evolution, and Natural Gas Accumulation in the Upper Paleozoic Tight Sandstones in the North Ordos Basin, China

Ren Wang [1,2], Kai Liu [1,2,*], Wanzhong Shi [1,2,*], Shuo Qin [1,2], Wei Zhang [3], Rong Qi [3] and Litao Xu [1,2]

[1] Key Laboratory of Tectonics and Petroleum Resources, Ministry of Education, China University of Geosciences, Wuhan 430074, China; rwang@cug.edu.cn (R.W.); qs@cug.edu.cn (S.Q.); litaoxu001@163.com (L.X.)
[2] School of Earth Resources, China University of Geosciences, Wuhan 430074, China
[3] Exploration and Development Research Institute, SINOPEC North China Company, Zhengzhou 450006, China; trzhangwei.hbsj@sinopec.com (W.Z.); qirong.hbsj@sinopec.com (R.Q.)
[*] Correspondence: lukai@cug.edu.cn (K.L.); shiwz@cug.edu.cn (W.S.)

Abstract: The vague understanding of the coupling relationship among natural gas charging, reservoir densification, and pressure evolution restricted the tight gas exploration in the Lower Shihezi Formation of the Hangjinqi area, north Ordos Basin. In this study, the quantitative porosity evolution model, the pressure evolution process, and the natural gas charging history of tight sandstone reservoirs were constructed by integrated investigation of the reservoir property, the thin section, SEM and cathode luminescence observations, the fluid inclusion analysis and the 1D basin modeling. The results show that the compaction and cementation reduced the primary porosity by 21.79% and 12.41%, respectively. The densification of the reservoir occurred at circa 230 Ma, which was before the natural gas charging time from 192 to 132 Ma. The paleo-overpressure within the tight reservoirs occurred since the Middle Jurassic with the pressure coefficients between 1.1 and 1.55. The continuous uplifting since the Late Cretaceous resulted in the under- and normal-pressure of the Lower Shihezi Formation with the pressure coefficients ranging from 0.67 to 1.05. The results indicate that the densification of the reservoirs was conducive to the formation of paleo-pressure produced by gas generating. The gas predominantly migrated vertically, driven by gas expansion force rather than buoyance and displaced the pore water in the reservoirs near source rocks.

Keywords: tight gas reservoirs; reservoir densification; pressure evolution; gas accumulation; Hangjinqi area; Ordos Basin

1. Introduction

The tight sandstone gas is an important unconventional hydrocarbon resource with widespread distribution and considerable potential over the world [1–5]. In recent years, the exploration and development of tight sandstone gas have made significant achievements in the Upper Paleozoic strata of the central and north Ordos Basin, accompanied by the discoveries of a lot of big gas fields with proven reserves over 100×10^9 m³ [6–9]. As more attentions were paid to margins of the basin, a large quantity of tight gas with geological reserves more than 700×10^9 m³ was found in the Upper Paleozoic coal-bearing successions in the Hangjinqi area [10].

It has been widely believed that the tight sandstone reservoirs in the Ordos Basin have been subjected to deep burial and complex diagenetic modifications, resulting in tiny pores and throats, strong heterogeneity, and poor physical properties with porosity and air permeability generally less than 10% and 1 mD [11–14]. Different relationship between reservoir densification and gas charging time would imply different types of tight sandstone reservoirs, accumulation mechanisms, and exploration strategies of the tight

sandstone gas [15,16]. The continuous or quasi-continuous gas accumulations tended to be formed when the reservoir densification occurred before gas charging, which were generally characterized by extensive distribution without distinct boundaries, complicated gas-water contacts and abnormal original reservoir pressure [2,11,16]. It is very difficult for the gas to migrate over long distance due to the great capillary resistance and strong heterogeneity in this type of tight reservoir [17]. In contrast, if the gas charging was prior to the sandstone densification, the gas was prone to migrating over long distance and accumulating in the structural highs because of the good reservoir properties, which is analogous to the conventional gas accumulations [15]. Afterwards, the reservoir became tight and the gas was generally still located near where the gas reservoirs were previously formed [16]. Although some researchers have studied the reservoir quality and its controlling factors [18,19], the porosity evolution and densification time of the Permian tight sandstone reservoirs are still unclear in the Hangjinqi area. The hydrocarbon charging time and accumulation process have been demonstrated by previous works [20,21], but their relationship with reservoir densification was not properly constrained in the research area. The types of tight sandstone reservoirs and gas accumulation mechanisms remained poorly understood, which restricted the further tight gas exploration in the Hangjinqi area.

In this study, the quantitative porosity evolution model of tight sandstone reservoirs in the Lower Shihezi Fm. was established by using the porosity data and petrography analysis methods. The pressure evolution history of tight reservoir was reconstructed by the combined analyses of inclusion thermodynamics simulation and 1D basin modeling. The coupling relationship among natural gas charging, reservoir densification, and pressure evolution were further analyzed. The results of our study can reveal the tight sandstone gas accumulation process in the Hangjinqi area, and may provide guidance and strategies for gas exploration in the Ordos Basin and other basins with similar geological conditions over the world.

2. Geological Settings

The Ordos Basin is a large intraplate remnant cratonic basin developed on the basement of the Archean and Proterozoic continental crust [22–24]. It is located in the western part of the North China Platform with low dip angle strata and relatively stable tectonics [24–26]. The basin consists of six structural units including the Yimeng Uplift, Weibei Uplift, Western Fold-Thrust Belt, Tianhuan Depression, Jinxi Flexural-Fold Belt, and Shanbei Slope (Figure 1B). The Hangjinqi area lies in the Yimeng Uplift of the northern Ordos Basin. Three big faults are developed in the middle of this region, with two nearly west-east-trending and one northeast-southwest-trending (Figure 1C).

The Upper Paleozoic strata in the study area include the Upper Carboniferous Taiyuan Formation (Fm.), Lower Permian Shanxi Fm., Middle Permian Lower and Upper Shihezi Fm., and Upper Permian Shiqianfeng Fm. in ascending order [10,27] (Figure 2). From the Taiyuan Fm. to the Shiqianfeng Fm., the depositional environment evolved from the marine facies, the paralic facies, the deltaic facies, and to the fluvial dominated continental facies [28–30]. Widespread coal seams in the Taiyuan Fm. and Shanxi Fm. are predominant source rocks with the maximum thickness of more than 30 m, which are mainly distributed in the south of the Hangjinqi area [20,21]. As the main gas-bearing layer, the Lower Shihezi Fm. recorded fluvial clastic deposits, which are mainly composed of pebbly sandstone, sandstone, and mudstone interbedding [18,31]. The Upper Shihezi Fm. and Shiqianfeng Fm. consist of fluvial and lacustrine deposits, providing an effective sealing for the Permian tight sandstone gas [17,22] (Figure 2).
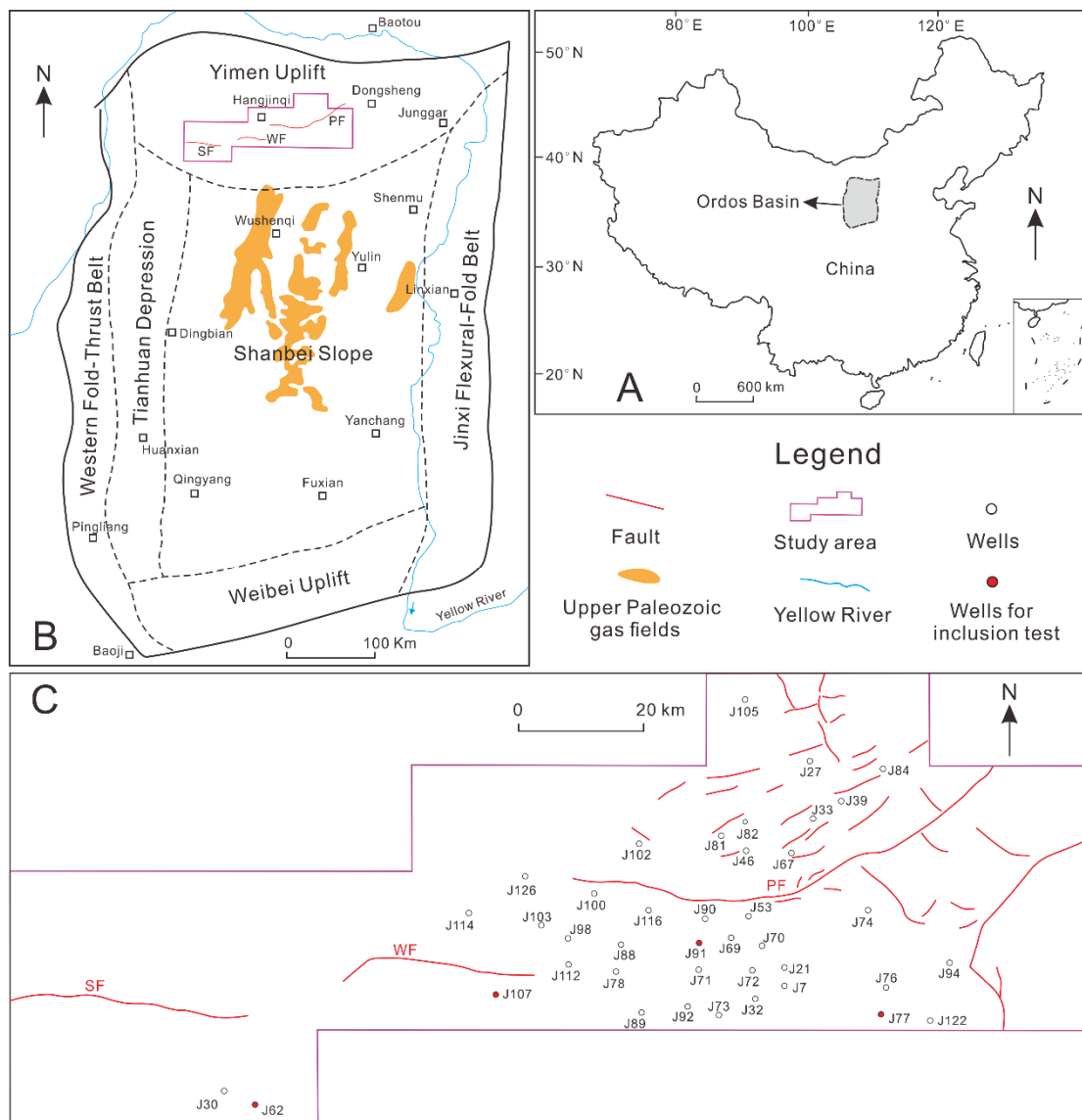
Figure 1. (**A**) Location map of the Ordos Basin in China; (**B**) Tectonic units and Upper Paleozoic gas fields in the Ordos Basin. Modified from Yang et al. (2015) [24]; (**C**) Drilling wells and main faults in the Hangjinqi area. PF: Porjiang-haizi fault; WF: Wulan-jilinmiao fault; SF: Sanyanjing fault.
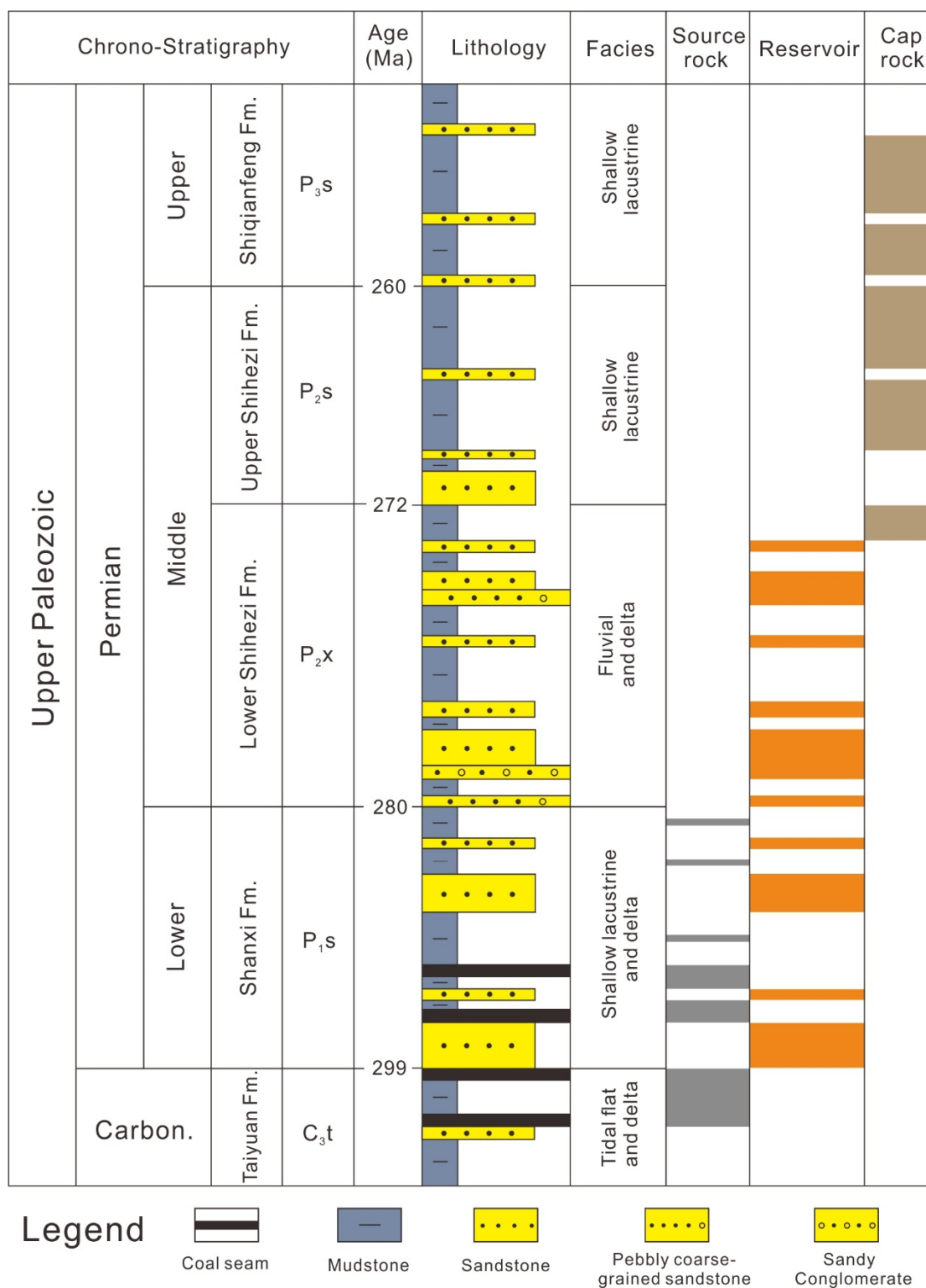
Figure 2. Generalized stratigraphy of the Upper Paleozoic successions in the Ordos Basin. Modified from Zhao et al. (2014) [32] and Wang et al. (2020) [18].

3. Data and Methods

In this study, the reservoir properties, detrital composition, pore types, and diagenetic characteristics of the Permian tight sandstones were firstly investigated by petrography observations. Then, the results obtained from the sandstone compositional analyses were used to quantitatively calculate the changes in porosity. According to the porosity change

resulting from different diagenetic processes and diagenetic sequence, the porosity evolution model was constructed and the reservoir densification process was analyzed. The gas charging time was determined by homogenization temperatures of fluid inclusions, and the pressure evolution history was constructed by fluid inclusion thermodynamic simulation and 1D basin modeling. After that, the relationship between reservoir densification and gas charging time was analyzed. Combined with the pressure evolution, the gas accumulation process and mechanism were eventually discussed.

3.1. Reservoir Characterization

Integrated analyses of the reservoir property, petrography, cathode luminescence, and scanning electron microscopy (SEM) were conducted on the core samples from the Lower Shihezi Fm.in the Hangjinqi area. More than 1000 core plugs with porosity and permeability values were collected from the North China Petroleum Bureau, Sinopec, to study the physical properties of the tight sandstone reservoirs. The porosity was measured with a helium porosimetry and the permeability was determined by using a pulse-decay permeameter with helium flowing and that calculated depending on total gas flux measurements.

A total of 250 thin sections were impregnated with alizarin red and potassium ferrocyanide for distinguishing the carbonate minerals, and part of them were stained with blue epoxy resin to sketch the pores. The textural data, detrital mineral composition, and thin section porosity for each type of pores were determined by counting 300 points on each sample. SEM and cathode luminescence analysis were combined to investigate the types and occurrence of different diagenetic minerals. The SEM analysis was carried out by a Quanta 450 FEG scanning electron microscope equipped with an energy dispersive spectrometer (EDS) in the State Key Laboratory of Geological Processes and Mineral Resources, China University of Geosciences. The cathode luminescence observation was undertaken by using a CL8200 MK5 detector equipped with a Leica DM2500 optical microscope.

3.2. Porosity Evolution Analyses

The results obtained from the petrography analyses were used to calculate the changes in porosity resulting from different diagenetic processes. The following parameters were calculated:

(1) Primary porosity, $\Phi_0 = 20.91 + 22.90/S_o$ [33], $S_o = (D_{25}/D_{75})^{1/2}$, where S_o is the Trask sorting coefficient, D_{25} and D_{75} are the corresponding particle diameter at cumulative content of 25 and 75%, respectively;

(2) Porosity after compaction, $\Phi_1 = C + \varphi_{pm} \times \varphi_p/\varphi_t$, where C is the total cement content, φ_{pm} represents the thin section porosity of the residual intergranular pores, φ_p is the core measured porosity, φ_t is total thin section porosity;

(3) Porosity reduction by compaction, $\Phi_2 = \Phi_0 - \Phi_1$;

(4) Porosity reduction by cementation, $\Phi_3 = C$;

(5) Porosity increase by authigenic inter-crystalline pores, $\Phi_4 = \varphi_i \times \varphi_p/\varphi_t$, where φ_i is the thin section porosity of authigenic inter-crystalline pores;

(6) Porosity after cementation, $\Phi_5 = \Phi_1 - \Phi_3 + \Phi_4$;

(7) Porosity increase by dissolution, $\Phi_6 = \varphi_d \times \varphi_p/\varphi_t$, where φ_d represents the thin section porosity of dissolution pores.

3.3. Fluid Inclusions Analysis

Microscopy, fluorescence spectroscopy, and micro-thermometry were conducted on the 19 sandstone samples of the Lower Shihezi Fm. from four wells (J62, J107, J91, and J77). The samples were doubly polished to thin sections with the thickness of approximately 100 μm. The fluid inclusions petrography, including inclusion type, occurrence, and fluorescence color, were observed by using a Nikon 80I dual-channel fluorescence microscope equipped with both transmitted and ultraviolet light sources, with the ultraviolet excitation wavelength of 365 nm. The measurement of homogenization temperature (HT) was undertaken by using a LinkamTHMS600 heating–freezing stage with the temperature precision

of ±0.1 °C. The heating rate was initially 10 °C/min and adjusted to 2 °C/min when the inclusions were close to a uniform state.

Petroleum inclusion thermodynamic modeling (PVTx) was used to estimate the pressure trapped within fluid inclusions in this study. The molar percentage of C_{7+} in the oil inclusion is closely correlated to the degree of bubble filling (Fv), and can be calculated by the following formula [34,35]:

$$C_{7+} = aF_v{}^b \times 100\% \tag{1}$$

where a and b, dimensionless, are the coefficients as a function of homogenization temperature of oil inclusion given by following formulas:

$$a = -1.81674 \times 10^{-8}T_h{}^4 + 7.49047 \times 10^{-6}T_h{}^3 - 9.20595 \times 10^{-4}T_h{}^2 + 6.52266 \times 10^{-2}T_h - 9.89904 \times 10^{-1} \tag{2}$$

$$b = 7.56250 \times 10^{-6}T_h{}^4 - 4.45141 \times 10^{-3}T_h - 4.12191 \times 10^{-1} \tag{3}$$

where T_h is homogenization temperature, °C. Then, the C_1 molar percent can be determined based on the C_{7+} molar percent of a single petroleum inclusion, as follows:

$$C_1 = -1.434 \times 10^{-7}C_{7+}{}^5 + 4.065 \times 10^{-5}C_{7+}{}^4 - 4.240 \times 10^{-3}C_{7+}{}^3 + 2.051 \times 10^{-1}C_{7+}{}^2 - 5.509 \times C_{7+}{}^1 + 1.080 \times 10^{-2} \tag{4}$$

Based on the C_1 molar percent and Th value, the isochore equation of the single oil inclusion can be established by the methodology of Ping et al., 2013 [34]. By combining the homogenization temperature of coeval aqueous inclusions with burial-thermal history, the trapping pressure values and corresponding timings when oil inclusions were captured can be determined.

3.4. 1D Basin Modeling

Burial, thermal, and pressure evolution histories were reconstructed by using the PetroMod 1D software (V. 2016). The stratum thickness and lithology were obtained from the cutting and logging data. Except for the source rock layers, each layer was mixed by the lithology mixing module of the software based on the lithology composition (Table 1). The Carboniferous-Permian source rock layers were set by pure lithology in order to simulate hydrocarbon generation pressure. The ages of depositional and erosional events were constrained by using the Chinese Stratigraphic Table (2014 edition) combined with the established local chronostratigraphic frameworks [24,32], and the erosion thickness was referenced from the results of Chen et al. (2006) [36]. The values of paleo-heat flow (PHF) in the Ordos Basin were mainly obtained from the works of Ren et al. (2017) [37]. The paleo-heat flow was relatively low in the Upper Paleozoic and increased drastically and reached its maximum as a result of a tectonic thermal event in the Late Jurassic and Early Cretaceous. Afterwards, the heat flow gradually decreased in the Cenozoic period. The sediment–water-interface temperature (SWIT) was calculated by an integrated PetroMod module based on the suggestion of Wygrala (1989) [38] (Table 1). The Easy% Ro model of Sweeney and Burnham (1990) [39] was used to calculate the organic matter maturity history. The thermal model was calibrated against the measured vitrinite reflectance (Ro) values and bottom-hole flow temperatures. The geochemical data of the coal seams were obtained from the North China Company, Sinopec. The average values of total organic carbon (TOC) and hydrogen index (HI) are 64.4% and 184.3 mg/g, while the average TOC and HI values of mudstones are 3.2% and 86.8 mg/g, respectively [40] (Table 1). The kinetic model of the Upper Paleozoic coal seams, called the Ordos Coal (2015), was established by laboratory pyrolysis experiments using a sealed gold tube system by Liu et al. (2016) [41]. The Pepper and Corvi (1995) _TIIIH (DE) kinetics was chosen for the mudstone (Table 1), because the Type III kerogen contains some high plants. Finally, the pressure evolution model was constrained by pressure via inclusion thermodynamic simulation and drill-stem test (DST). The DST data of the Upper Paleozoic strata were collected from the North China Company, Sinopec.

Table 1. Input parameters for 1D basin modeling. SWIT: Sediment-water-interface temperatures. PHF: Paleo-heat flow. HI: Hydrogen index. The "Ordos coal (2015)" kinetics was referenced from Liu et al. (2016) [41].

Formation	Deposition Age		Erosion Age		Lithology	PSE	SWIT (°C)	PHF (Mw/m²)	TOC (%)	Kinetics	HI (mg/gTOC)
	From (Ma)	To (Ma)	From (Ma)	To (Ma)							
N-Q	7.4	0			Shale (organic lean, sandy)	Overburden	15.33	53			
K	145	96	96	7.4	Sandstone & Shale	Overburden	25	70			
J$_2$	175	161	161	145	Sandstone & Shale	Overburden	20	62			
J$_1$	195	179	179	175	Sandstone & Shale	Overburden	19.02	59			
T	251	206	206	195	Sandstone & Shale	Overburden	21.37	57			
P$_3$s	260	251			Shale & Sandstone	Cap rock	20	56			
P$_2$s	272	260			Shale & Sandstone	Cap rock	17.16	55			
P$_2$x	280	272			Sandstone & Shale	Reservoir	17.48	54			
P$_1$s	288	280			Sandstone (clay rich)	Reservoir	18.24	53			
C$_3$-P$_1$_Coal	291	288			Coal (pure)	Source rock	19	53	64.4	Ordos Coal (2015)	184.3
C$_3$-P$_1$_Mud	304	291			Shale (organic rich, 3% TOC)	Source rock	21.26	52	3.2	Pepper & Corvi (1995) _TIIIH (DE)	86.8

4. Results

4.1. Characteristics of the Tight Reservoirs

The 1208 tight sandstone samples from the Lower Shihezi Fm. show poor reservoir quality. The porosity ranges from 0.69% to 19.6% with an average of 9.58%, while the permeability varies between 0.006 mD and 10.3 mD, averaging 0.95 mD (Figure 3). The averaged porosity and permeability are less than 10% and 1 mD, respectively, suggesting that the sandstones are typical tight reservoirs (Zou et al., 2012; Dai et al., 2012) [3,8].
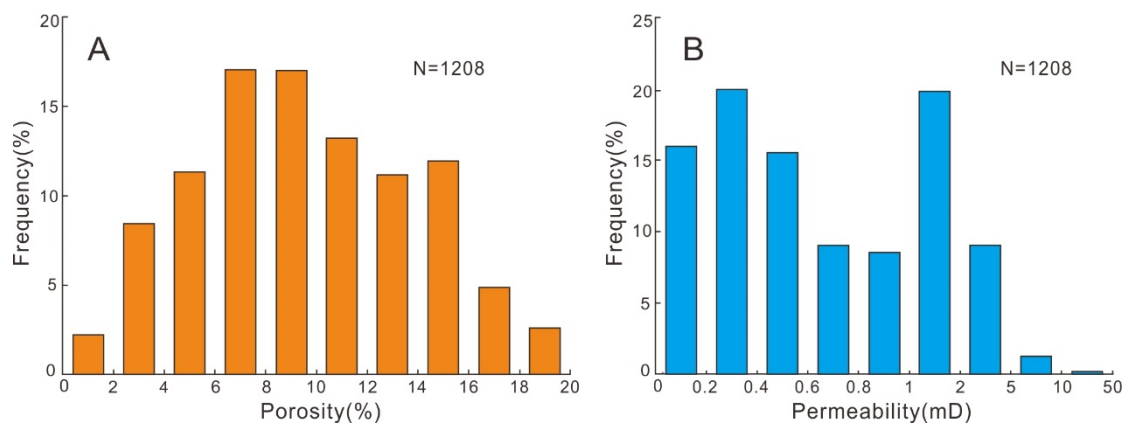

Figure 3. Histogram of the porosity (**A**) and permeability (**B**) of the sandstone in the Lower Shihezi Fm., Hangjinqi area.

The sandstones of the Lower Shihezi Fm. are mainly composed of litharenite, sublitharenite, and a small amount of feldspathic litharenite (Figure 4). In the detrital components, the contents of quartz, rock fragment, and feldspar range from 50% to 92% (avg. 69.09%), 8% to 48% (avg. 28.04%), and 0 to 15% (avg. 2.23%), respectively. The rock fragments mainly consist of metamorphic rock fragments (avg. 22.36%), followed by a small quantity of igneous rock fragments (avg. 3.56%) and sedimentary rock fragments (avg. 2.12%). The cements are dominated by authigenic clay minerals and carbonates, with an average content of 12.41%. The sandstones are predominantly medium- and coarse-grained with moderately sorting and sub-angular rounding, reflecting a medium structural maturity.

The pore types of the sandstones in Lower Shihezi Fm. are dominated by dissolution pores (intergranular and intragranular pores), intercrystalline pores, and microfractures, with rare residual intergranular pores. Dissolution pores are mainly formed by partial to complete dissolution of the feldspar grains and rock fragments as a result of organic acid-rich fluids (Figure 5A–C). Intercrystalline pores mainly exist in the authigenic kaolinite, which is usually the transformation byproduct of the feldspar dissolution [42] (Figure 5E). The microfractures are predominantly composed of structural microfractures and diagenetic microfractures (Figure 5D), in which the latter usually occur along the grain edge or within the rigid grains (Figure 5B,C,F).

4.2. Quantitative Characteristics of Porosity Evolution

The sorting coefficients of tight sandstones in the Lower Shihezi Fm. range from 1.57 to 1.93 with an averaged value of 1.72, and therefore, the primary porosity ranges from 32.77% to 35.49% with the average of 34.21%. The calculated porosity of the sandstones after compaction ranges from 2% to 29% with an average of 12.42%, showing that the compactional porosity loss is approximately 21.79%. the porosity after cementation varies between 0 to 0.48%, averaging 0.01%, demonstrating that the cementational porosity loss is 12.41%. Additionally, porosity increasing through dissolution ranges from 1.57% to 9.58% with an averaged value of 8.56%, which accounts for 25% of the primary porosity. The

average value of porosity that provided by microfractures and intercrystalline pores is 0.16% and 0.85%, respectively.
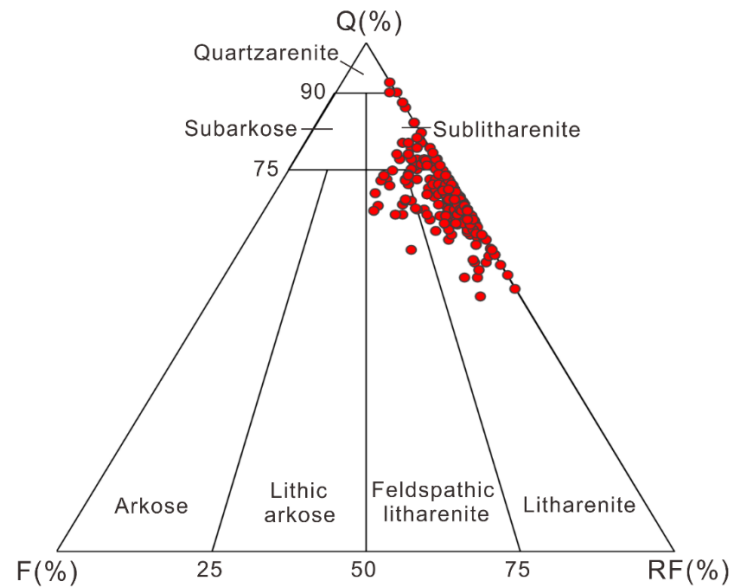

Figure 4. Composition diagram of the sandstone reservoirs in the Lower Shihezi Fm. in the Hangjinqi area, Q: quartz; F: feldspar; RF: rock fragment. (Number of samples = 250).
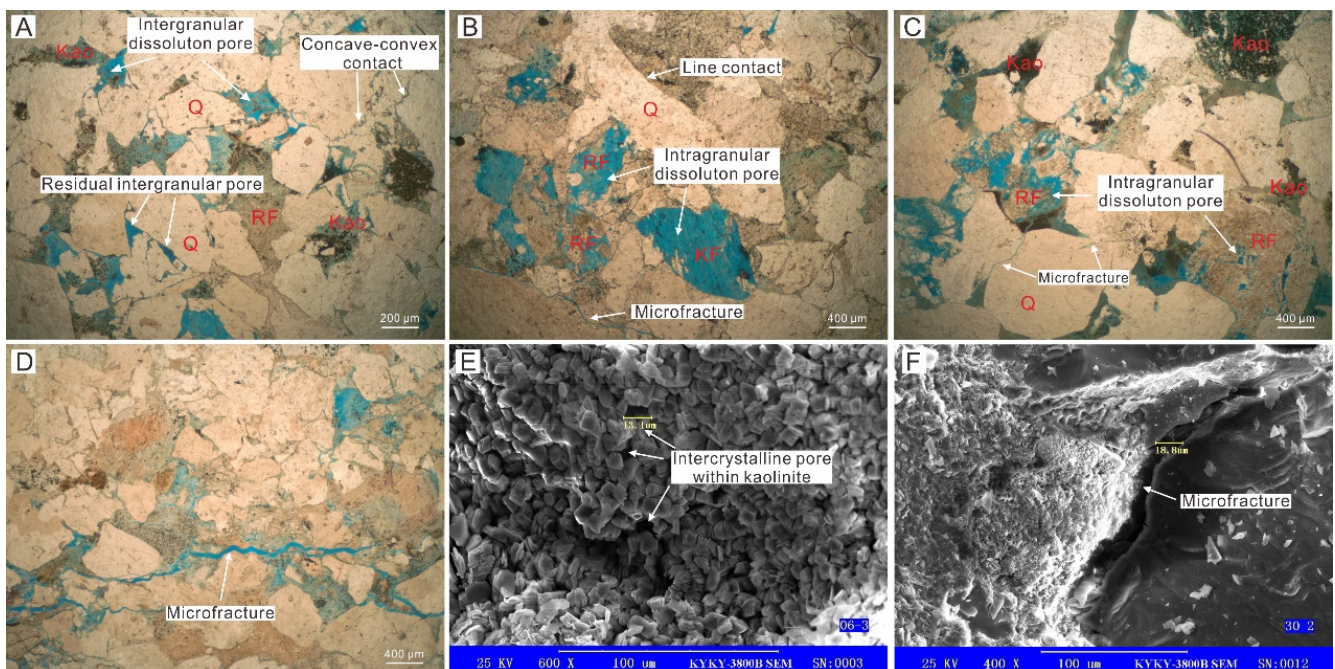

Figure 5. Microscopy and SEM observation showing the types of sandstone reservoir space in the Lower Shihezi Fm. (**A**) Well J103, 3096.57 m, medium-grained sandstone; (**B**) Well J103, 3081.06 m, coarse-grained sandstone; (**C**) Well J105, 2163.99 m, coarse-grained sandstone; (**D**) Well J114, 3018.72 m, medium-grained sandstone; (**E**) Well J89, 3082.34 m, fine-grained sandstone; (**F**) Well J92, 3061.25 m, medium-grained sandstone. Q: quartz; RF: rock fragment; KF: K-feldspar; Kao: kaolinite.

4.3. Fluid Inclusions

The fluid inclusions in the Lower Shihezi Fm. are very abundant and dominated by aqueous inclusions and hydrocarbon-bearing aqueous inclusions, with a small number

of hydrocarbon inclusions. The inclusions are mostly observed in the healed crack of quartz grain as groups of beads or bands and in shapes of near circle, elliptical, or irregular, with few in the quartz overgrowth and calcite cement. The aqueous inclusions and hydrocarbon-bearing aqueous inclusions, accounting for 80~90% of the total, are colorless and transparent under transmitted light and no fluorescence under ultraviolet light. The diameters of these inclusions are generally smaller than 20 μm with the main peak values of 5~15 μm. The gas-liquid ratio is mainly 2~8% and generally less than 10%. The hydrocarbon inclusions make up 10~20% of the total, including oil inclusions and gas inclusions. The oil inclusions are mainly brown or light brown under transmitted light and show blue or blue-green fluorescence under ultraviolet light (Figure 6A,B), reflecting a medium-high thermal maturity of organic matter [43]. The diameters and gas–liquid ratios of oil inclusions are mostly 6~12 μm and 4~12%, respectively. The gas inclusions are mainly gas-only phase and gas-liquid two-phase, and show dark or dark grey color under transmitted light and no fluorescence under ultraviolet light (Figure 6C,D). The homogenization temperatures of aqueous inclusions coexisting with hydrocarbon inclusions from wells J62, J107, J91, and J77 range from 70 °C to 160 °C, with the main peak values of 90~120 °C (Figure 7). The characteristics of hydrocarbon inclusions and homogenization temperatures of coeval aqueous inclusions from typical samples are partially listed in Table 2.
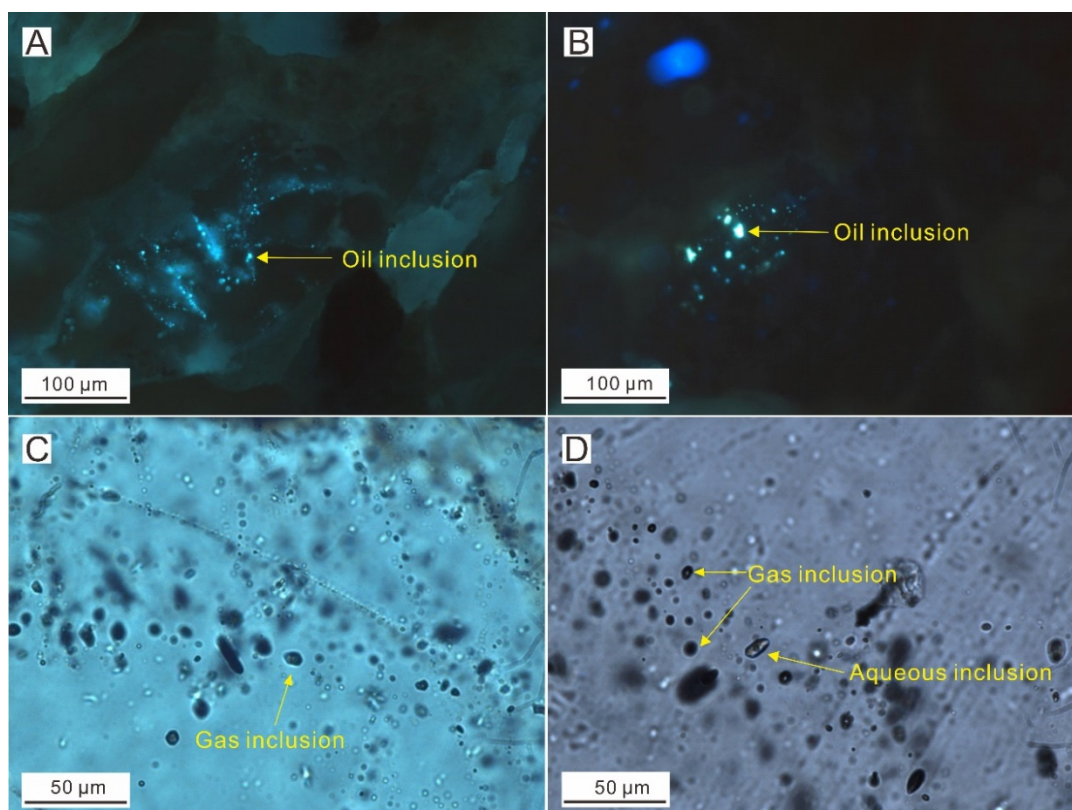

Figure 6. Photomicrographs of the hydrocarbon inclusions from the Lower Shihezi Fm. in the Hangjinqi area, north Ordos Basin. (**A**) Oil inclusions with blue fluorescence under ultraviolet light, Well J77, 2698.75 m; (**B**) Oil inclusions with blue-green fluorescence under ultraviolet light, Well J77, 2698.75 m; (**C**) Gas inclusions with dark grey color under transmitted light, Well J77, 2709.65 m; (**D**) Gas inclusion and coeval aqueous inclusion under transmitted light, Well J62, 3468.78 m.
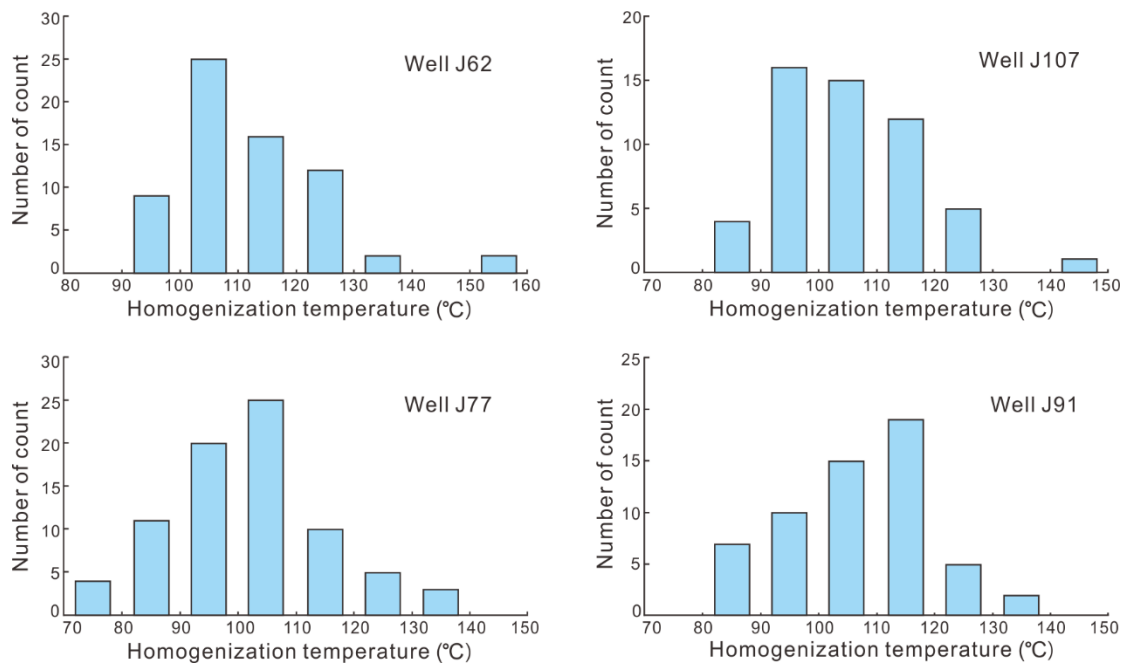
Figure 7. Histograms of homogenization temperatures of aqueous inclusions coexisting with hydrocarbon inclusions from the sandstones in the Lower Shihezi Fm.

Table 2. Characteristics of the hydrocarbon inclusions from the Lower Shihezi Fm. in the Hangjinqi area, north Ordos Basin. GI: gas inclusion; OI: oil inclusion; AI: aqueous inclusion.

Well	Depth (m)	Type of HI	Location	Size (μm)	Fluorescence Color	HT of AI (°C)
J62	3468.78	GI	Crack across quartz	5	–	113.8
J62	3468.78	GI	Crack across quartz	6	–	112.9
J62	3468.78	GI	Crack within quartz	10	–	106.9
J62	3468.78	OI	Crack within quartz	7	blue	105.3
J62	3468.78	OI	Crack within quartz	12	blue	103.9
J62	3468.29	GI	Crack within quartz	8	–	133.5
J62	3468.29	GI	Crack within quartz	10	–	116.5
J107	3196.31	OI	Crack within quartz	9	blue	96
J107	3196.31	OI	Crack within quartz	7	blue	100.8
J107	3200.69	GI	Crack within quartz	16	–	99.3
J107	3200.69	GI	Crack within quartz	13	–	117.5
J107	3200.69	GI	Crack within quartz	12	–	109.3
J91	2978.06	GI	Crack within quartz	16	–	111.5
J91	2978.06	GI	Crack within quartz	5	–	118.1
J91	2978.06	GI	Crack within quartz	8	–	115.9
J91	2989.95	OI	Crack within quartz	7	blue	101.8
J91	2989.95	OI	Crack within quartz	6	blue	90.1

Table 2. *Cont.*

Well	Depth (m)	Type of HI	Location	Size (µm)	Fluorescence Color	HT of AI (°C)
J77	2706.62	OI	Crack within quartz	7	blue	101.9
J77	2706.62	OI	Crack within quartz	13	blue	132.9
J77	2713.3	OI	Crack within quartz	11	blue-green	83.3
J77	2713.3	OI	Crack within quartz	7	blue-green	81.9
J77	2713.3	GI	Crack within quartz	8	–	105.1
J77	2713.3	GI	Crack across quartz	12	–	90.3

4.4. Pressure Evolution History

Based on the 105 DST pressure values, the pore pressures of the Upper Paleozoic sandstones in the Hangjinqi area range from 13.8 Ma to 33.04 Ma, with the pressure coefficient (defined as the ratio of the pore pressure to hydrostatic pressure) ranging from 0.67 to 1.05 (avg. 0.87) (Figure 8). In this study, the formation with a pressure coefficient of more than 0.96 but less than 1.06 is considered as normal pressure [44]. Therefore, the Upper Paleozoic reservoirs mainly display an underpressure (91.43%) and some areas with normal pressure (8.57%). The pore pressures show a gentle decreasing trend with increasing depth, and different successions have a similar pressure gradient (Figure 8).
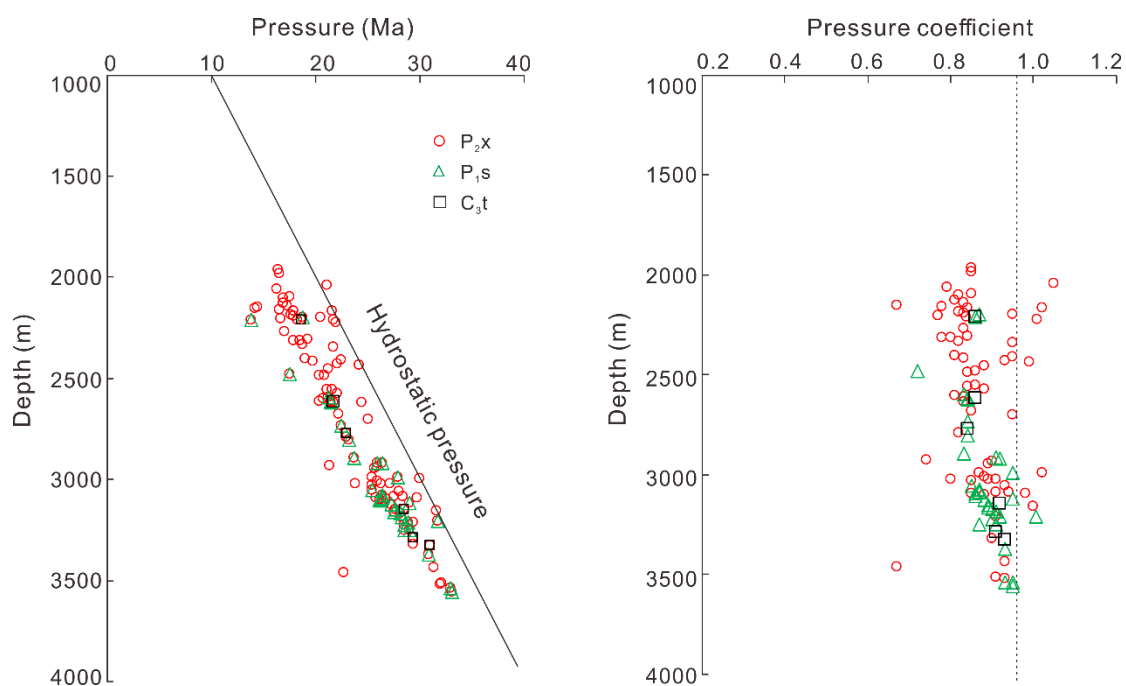

Figure 8. The current pressures and pressure coefficients of the Upper Paleozoic sandstones in the Hangjinqi area.

The trapping pressure of oil inclusions could be determined based on the F_v, Th_{oil}, Th_{aqu}, and C_{7+} and C_1 molar percentages. The inclusions information, paleo-pressure calculation parameters and results from the well J77 were listed in Table 3. Restrained by these paleo-pressure values and currently measured pressure data, the pressure evolution history of the well J77 was reconstructed by numerical modeling (Figure 9). The result shows that the sandstone reservoirs of the Lower Shihezi Fm. began to develop overpressure during the Middle Jurassic. The pore pressure decreased during the Late Jurassic as a result of the uplifting event. During the Early Cretaceous (ca. 143–121 Ma),

the pore pressure continued to increase from approximately 27.53 to 37.28 MPa, with the corresponding pressure coefficients ranging from 1.1 to 1.33. The pore pressure increased to a maximum value at about 49.5 MPa with the pressure coefficient of 1.55 at the end of the Early Cretaceous (ca. 96 Ma). Afterwards, the pressure decreased sharply for a long period due to sustained uplift and reached a low value of 23.2 Ma in the present day according to the DST data, with the approximately pressure coefficient at 0.84 (Figure 9).

Table 3. Parameters and calculated results of the oil inclusion trapping pressures for the sandstones in the Lower Shihezi Fm. from the well J77 in the Hangjinqi area. Fv: Degree of bubble filling, Pt: Trapping pressure, PC: Pressure coefficient.

| Fluorescence Color	Position	Th_{oil} (°C)	Fv (%)	Th_{aqu} (°C)	C_{7+} Molar Percent (%)	C_1 Molar Percent (%)	Pt (MPa)	Time (Ma)	Paleo-Depth (m)	PC
bule	crack within quartz	83.1	6	102.7	40.7	33.1	26.67	168	2358	1.1
bule	crack within quartz	91.9	6	134.3	44.9	29.1	37.29	121	2769	1.32
bule	crack within quartz	84.5	6.2	110.3	40.4	33.4	30.33	138	2495	1.19
bule	crack across quartz	78.4	4.8	103.1	45.2	28.9	27.53	142	2414	1.11
blue-green	crack within quartz	74.4	5	81.9	41.9	32	18.78	219	1774	1.03
bule	crack within quartz	72.6	4	87.3	47.8	26.4	20.3	213	1944	1.01
bule	crack within quartz	85.3	6.8	106.7	38.2	35.3	28.94	140	2455	1.15
bule	crack within quartz	88.6	7.3	99.6	37.6	35.8	23.46	185	2210	1.03
bule	crack within quartz	92.4	10	118.7	30.7	41.7	35.33	132	2590	1.33
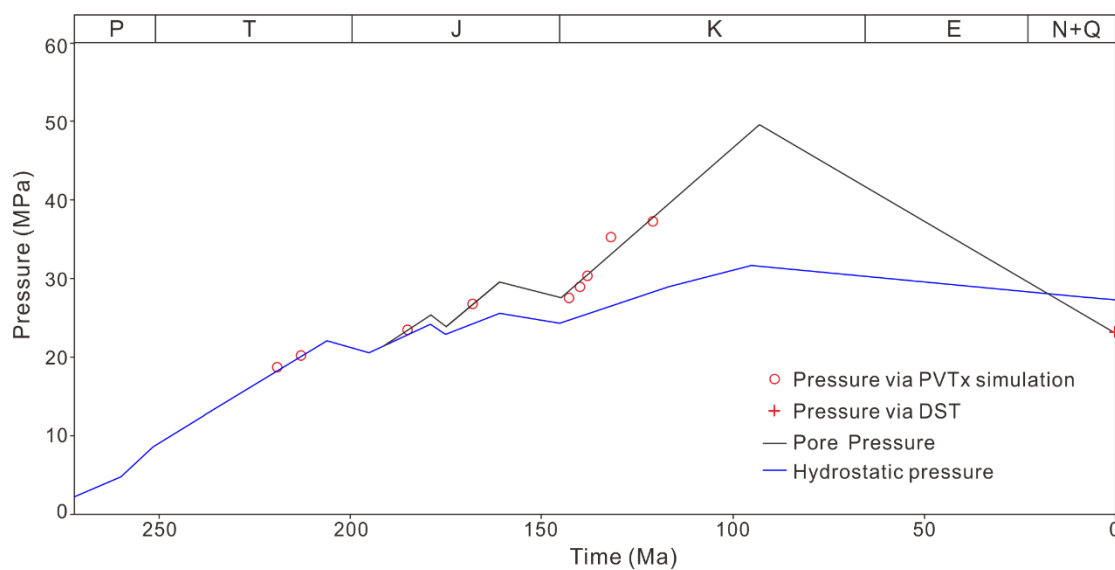
Figure 9. Pressure evolution of the well J77 via inclusion thermodynamic simulation and 1D basin modeling.

5. Discussion

5.1. The Densification of Sandstone Reservoir

The homogenization temperatures of aqueous inclusions coexisting with hydrocarbon inclusions in the sandstones of Lower Shihezi Fm. range from 70 °C to 160 °C (Figure 7). The source rocks in the study area recorded a medium-high maturation with Ro values ranging from 1.07% to 1.36%, and have temperature peaks of rock pyrolysis varying between 455 °C to 486 °C [21]. Additionally, the smectite content constitutes 15 to 26% of the mixed-layer illite/smectite (I/S) in the sandstones of Lower Shihezi Fm. in the Hangjinqi area [18]. All the above information indicates that the reservoirs have evolved into the mesodiagenetic B stage [45,46]. By combining the porosity evolution analysis with the diagenetic sequence, the densification process of the sandstone reservoirs in the Lower Shihezi Fm. can be revealed (Figure 10).
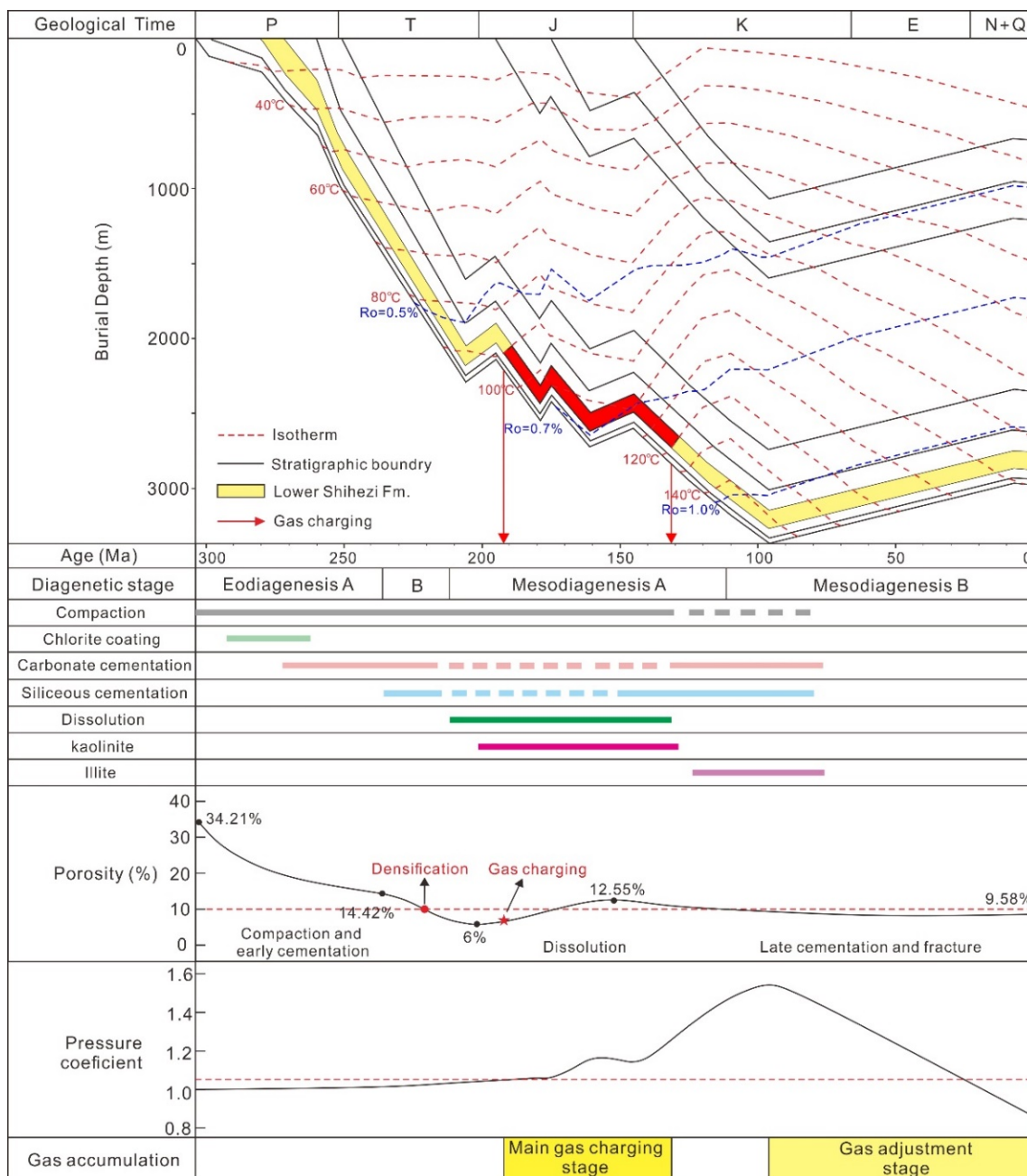
Figure 10. Comprehensive diagram showing the densification process, pressure evolution, and gas accumulation of the sandstone reservoir in the Lower Shihezi Fm., Hangjinqi area.

The eodiagenesis A stage corresponds to the burial depth of approximately 0–1250 m, in which the predominant diagenetic modification is mechanical compaction. The porosity was rapidly reduced in this period, characterized by grains line contacts, rearrangement and repacking of detrital grains, and pseudoplastic deformation of soft rock fragments [47,48] (Figures 5B and 11A). The intensity of mechanical compaction is closely related to the detrital composition [49,50]. The ductile debris, such as phyllite, killas, and mudstone debris constitute 43% of the rock fragments [51], leading to strong mechanical compaction in the sandstones of the Lower Shihezi Fm. (Figure 11A). The reservoirs evolved into the eodiagenesis B stage at a depth of approximately 1250–1920 m, in which the early cementation (mainly calcite and early quartz overgrowth) and chemical compaction played a profound role on porosity reduction. The calcite cements commonly fill in large intergranular spaces in the form of a poikilitic texture and display bright orange-red and yellow luminescence

patterns under the cathode luminescence [48] (Figure 11B). The chemical compaction is mainly indicative of concave-convex contacts between quartz grains, which can probably provide some sources of silica for the quartz overgrowth [52] (Figures 5A and 11E). By the end of this stage, the reservoir quality of the Lower Shihezi Fm. was severely deteriorated with the porosity reducing from 34.21 to 6%, and the densification of the reservoir occurred in the Late Triassic (ca. 230 Ma). When the reservoirs entered into the mesodiagenetic A stage, the coal-bearing source rocks matured and released massive organic acidic fluid, resulting in the dissolution of feldspar and unstable components in the rock fragments. The physical properties of the reservoir were prominently approved by dissolution with the porosity enhancement of approximately 8.56%. Nevertheless, the dissolution of feldspar would produce large amounts of kaolinite [42], which commonly occurred as pore-filling cements (Figure 11C). Additionally, the other late-stage cements including ferro-calcite, authigenic quartz, and authigenic illite further filled in the residual primary pores and secondary pores, causing the porosity degradation of approximately 6% (Figure 11D–F). The intercrystalline pores related to the authigenic clay minerals (especially kaolinite) and fractures produced after the Late Cretaceous have limited contribution to the porosity increase. As the strata uplifted and temperature decreased, the late cementation became weak and the porosity gradually evolved to 9.58%.
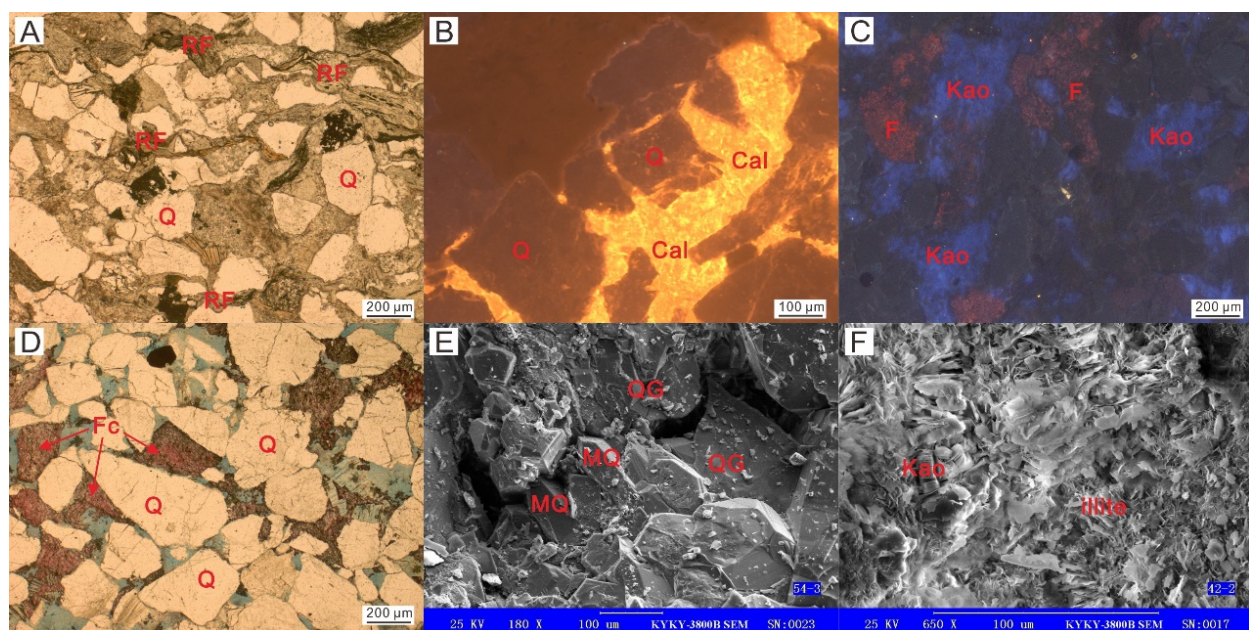

Figure 11. Photomicrographs recording the diagenesis of the Lower Shihezi reservoirs in the Hangjinqi area, north Ordos Basin. (**A**) Pseudoplastic deformation of soft rock fragments, well J103, 2696.86 m, plane-polarized light; (**B**) Calcite cements filling in the large pores with poikilitic texture, well J103, 3081.33 m, CL; (**C**) Feldspar dissolution and pore-filling kaolinite, well J103, 2987.21 m, CL; (**D**) Ferrocalcite cements filling in the relatively small pores, well J62, 3455.94 m, CL; (**E**) Quartz overgrowth and micro quartz, well J89, 3164.48 m, SEM. (**F**) Illite and kaolinite filling in the pores, well J92, 3066.1 m, SEM. Q = Quartz; RF = Rock fragments; Cal = Calcite; F = Feldspar; Kao = Kaolinite; Fc = Ferrocalcite; QG = Quartz overgrowth; MQ = Micro quartz.

The homogenization temperatures of the aqueous inclusions coexisting with hydrocarbon inclusions in the Lower Shihezi Fm. from four wells mainly range from 90 °C to 120 °C (Figure 7). Combined with burial-thermal history, the hydrocarbon accumulation was a continuous long-term process from the Early Jurassic to the Early Cretaceous (ca. 192 Ma–132 Ma) in the Hangjinqi area. The porosity of the sandstones in the Lower Shihezi Fm. was significantly below 10% during the Late Triassic (ca. 230 Ma), indicating that the reservoirs had already been sufficiently tight before the hydrocarbon charging.

5.2. Origin of the Abnormal Pressure

The disequilibrium compaction, tectonic compression, and fluid expansion have been considered as the major overpressure generation mechanisms in sedimentary basins [53]. The fluid expansion overpressure is mainly originated from hydrocarbon generation, thermal cracking of oil to gas, and aquathermal expansion [54]. The paleo-pressure in the Upper Paleozoic shales of the Ordos Basin has been identified to be derived from the fluid expansion based on multiple logging data [54,55]. Additionally, the low sedimentation rate of the Upper Paleozoic strata with an average value of less than 30 m/Ma was unfavorable to the formation of disequilibrium compaction overpressure in the study area (Figure 10) [55–57]. Frequent interbedding of mudstones and sandstones is not conducive to the formation of disequilibrium compaction overpressure (Figure 2). The grains in tight sandstone of the Lower Shihezi Fm. are dominant by line and concave-convex contacts, indicating that the mechanical compaction was strong and the disequilibrium compaction did not occur. The coal-bearing source rocks entered into the threshold of generating gas with the Ro more than 0.7% during the Early Jurassic (Figure 10). The paleo-overpressure in the Lower Shihezi Fm. occurred in the Middle Jurassic, whose formation time was consistent with the gas generation, suggesting that the gas generating by III-type kerogen probably played a significant role on the formation of paleo-overpressure [58]. The highest paleo-temperature of the formations in the study area was lower than the oil-cracking start temperature of 160 °C (Figure 10) [59], indicating that the cracking of oil contributes little to the overpressure generation. Additionally, the pressurization resulting from aquathermal expansion is generally mild and negligible [60]. The overpressure in the Lower Shihezi Fm was obviously derived from the pressure that were transferred from the underlying sources rocks.

The Ordos Basin continued to uplift as a result of the subduction of the paleo-Pacific Plate and Indian Plate since the Late Cretaceous [24]. It is widely accepted that the current underpressure and normal pressure in the Upper Paleozoic strata were the results of large-scale tectonic uplifting and denudation [16,55,61,62]. The temperature decrease, pore rebound, and natural gas dissipation during the uplifting stage were the main causes of the depressurization [55,63]. The pore fluid contracts more than the rock skeleton with the temperature decreasing, thus resulting in the reduction of the pore pressure [64]. The stratum uplifting and denudation can lead to unloading of overburden pressure, which will increase the pore space and reduce the pore pressure [65]. Therefore, the depressurization resulting from pore rebound was closely related to the erosion thickness of the stratum [62,63]. The pore pressure in the sandstones decreased more intensively than that in the mudstones due to pore rebound, forming a pressure difference between source rock layers and reservoirs to promote gas expulsion and charging during the uplifting stage [61]. The natural gas dissipation caused by gas expansion and diffusion played a significant role on the pressure reduction and gas adjustment and re-accumulation in the uplifting stage since the Late Cretaceous [55]. The formation of the Upper Permian secondary gas reservoirs was regarded as the result of gas expansion during the late-stage uplifting period in the northeast Ordos Basin [55,66].

5.3. Coupling among the Reservoir Densification, Pressure Evolution, and Natural Gas Accumulation

The porosity of the sandstone reservoirs in the Lower Shihezi Fm. was reduced below 10% by intensive compaction and early cementation during the Late Triassic (ca. 230 Ma) (Figure 10). The tightness of the reservoirs was conducive to the formation of paleo-overpressure produced by gas generating, because large amounts of natural gas was difficult to migrate over long distances and could be retained in the earlier formed tight reservoir [16]. The gas predominantly migrated vertically through the microfractures driven by gas expansion force from the source rocks and displaced the pore water in the near source rock reservoir [67]. Therefore, the hydrocarbon generation intensity and effective assemblages of source rocks and reservoirs are crucial for the gas accumulation of

tight reservoirs [17]. Additionally, the consequent dissolution of feldspars and rock fragments greatly approved the reservoir properties, providing available spaces and favorable migration paths for natural gas (Figure 10). The large-scaled charging of natural gas from the Early Jurassic to the Early Cretaceous (192–132 Ma) probably changed the formation water composition and inhibit the diagenesis of the sandstone reservoirs [68], such that the formation efficiency of fluid inclusions was slowed down [69]. Therefore, the proportion of fluid inclusions with the high homogeneous temperature (>120 °C) is relatively low in the Lower Shihezi Fm. (Figure 7).

The continuous tectonic uplifting since the Late Cretaceous had a profound influence on the gas accumulation and re-enrichment in the north Ordos Basin [55,66]. The uplifting and erosion of the Ordos Basin resulted in large-scaled natural gas loss and formation pressure release. Although the porosity of the sandstone reservoirs in the Lower Shihezi Fm. had been reduced again by late-stage cementation, a large number of structural fractures were formed due to uplifting and beneficial to the gas migration [61] (Figure 12). The gas charging from source rock to the reservoir was limited because of the decreasing temperature and weak hydrocarbon generating, but adjustment and re-accumulation of the primary gas reservoirs were dominant during this period in the north Ordos Basin. Divided by the Porjianghaizi fault, the strata in the northern part of the study area was uplifted and eroded more intensively than the southern part [21], forming a pressure difference between northern and southern part. The primary gas reservoirs in the southern part were destroyed and migrated laterally to the north, driven by the gas expansion force and buoyance [21]. Additionally, the intense collision of the Indian and Eurasian Plate during the Middle to Late Eocene resulted in large-scale strike-slip movement in the Ordos Basin and reactivated the faults in the study area [24]. The NS-trending superimposed sandy bodies in the Shanxi and Lower Shihezi Fms. and laterally connected areas of Porjianghaizi fault provided migration pathways for natural gas [26]. Part of the natural gas eventually accumulated in the low amplitude anticlinal structure through small-scaled faults in the northern part [21].
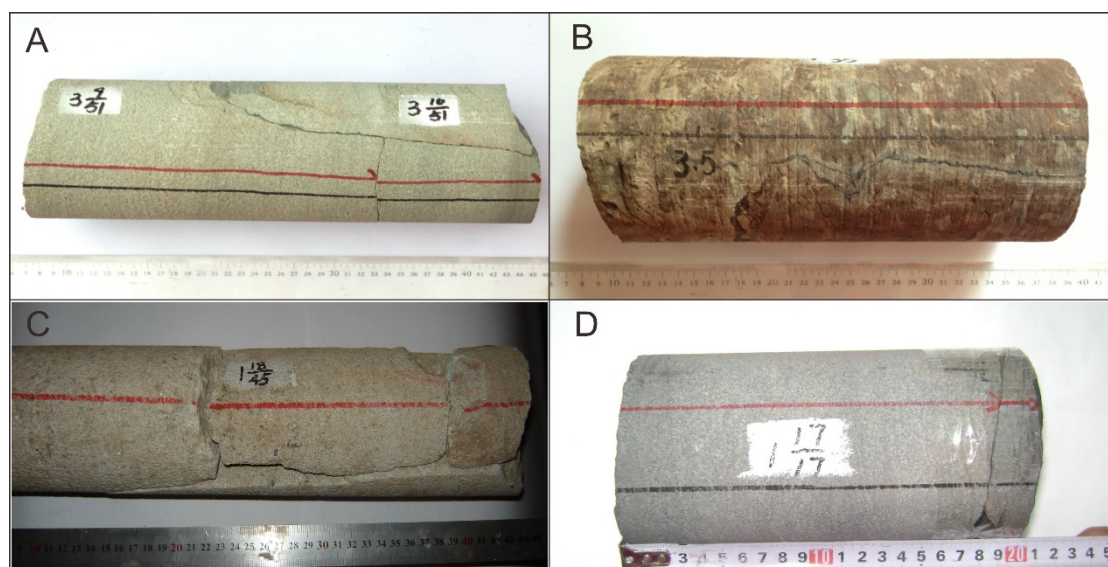

Figure 12. Core photos showing the characteristics of fractures in the Lower Shihezi Fm. (**A**) Well J107, 3193.26–3193.61 m, medium-grained sandstone; (**B**) Well J107, 3137.26–3137.50 m, mudstone; (**C**) Well J62, 3457.41–3457.85 m, pebbly coarse-grained sandstone; (**D**) Well J91, 2953.96–2954.15 m, fine-grained sandstone.

6. Conclusions

(1) The sandstone reservoirs of the Lower Shihezi Fm. are generally tight with average porosity and permeability of 9.56% and 0.95 mD, respectively. The pore spaces are mainly composed of dissolution and intercrystalline pores within authigenic kaolinite, rare primary pores, and a small amount of microfractures. The compaction and cementation, respectively, resulted in the porosity loss at 21.8 and 12.41%, while the dissolution increased the porosity by 8.56%. The reservoir was significantly tightened by strong mechanical compaction and early cementation during the Late Triassic (ca. 230 Ma), which was prior to the large-scale gas charging since the Early Jurassic (ca. 192 Ma).

(2) The sandstone reservoir of the Lower Shihezi Fm. began to develop overpressure during the Middle Jurassic, which originated from the fluid expansion caused by gas generating. The gas expansion force was the main driving force for gas charging during the Early Jurassic to the Early Cretaceous (ca. 192–132 Ma). The continuous tectonic uplifting since the Late Cretaceous resulted in the underpressure and normal pressure of the Lower Shihezi Fm. The temperature decrease, gas expulsion, and pore rebound during the uplifting stage were the main causes for the depressurization. The gas expulsion during this period played a significant role in the gas charging and re-accumulation in the northern Ordos Basin.

(3) The reservoir densification occurred before the hydrocarbon charging, implying that the gas accumulation in the study area is continuous or quasi-continuous. The densification of the reservoir was conducive to the formation of the paleo-pressure caused by gas generation during the main gas charging stage. The gas predominantly migrated vertically driven by gas expansion force rather than buoyance and displaced the pore water in the reservoirs near source rocks. Therefore, the hydrocarbon generation intensity and effective assemblages of source rock and reservoir are crucial for the gas accumulation and exploration of this type of tight reservoirs.

Author Contributions: Conceptualization, R.W. and K.L.; methodology, R.W.; software, K.L.; validation, R.W., K.L. and W.S.; formal analysis, S.Q.; investigation, L.X.; resources, W.Z.; data curation, R.Q.; writing—original draft preparation, R.W.; writing—review and editing, K.L.; visualization, R.W.; supervision, W.S.; project administration, W.S.; funding acquisition, W.S. All authors have read and agreed to the published version of the manuscript.

Institutional Review Board Statement: Not applicable.

Informed Consent Statement: Not applicable.

Data Availability Statement: The data relevant with this study can be accessed by contacting the corresponding author.

Conflicts of Interest: The authors declare no conflict of interest.

References

1. Law, B.E.; Curtis, J.B. Introduction to unconventional petroleum systems. *AAPG Bull.* **2002**, *86*, 851–1852.
2. Schmoker, J.W. Resource assessment perspectives for unconventional gas systems. *AAPG Bull.* **2002**, *86*, 1993–2000.
3. Zou, C.N.; Zhu, R.K.; Liu, K.Y.; Su, L.; Bai, B.; Zhang, X.X.; Yuan, X.J.; Wang, J.H. Tight gas sandstone reservoirs in China: Characteristics and recognition criteria. *J. Pet. Sci. Eng.* **2012**, *88*, 82–91. [CrossRef]
4. Mcglade, C.; Speirs, J.; Sorrell, S. Unconventional gas—A review of regional and global resource estimates. *Energy* **2013**, *55*, 571–584. [CrossRef]

5. Li, G.Z.; Qin, Y.; Shen, J.; Wu, M.; Li, C.; Wei, K.H.; Zhu, Z. Geochemical characteristics of tight sandstone gas and hydrocarbon charging history of Linxing area in Ordos Basin, China. *J. Pet. Sci. Eng.* **2019**, *177*, 198–207. [CrossRef]
6. Yang, H.; Fu, J.H.; Wei, X.S.; Liu, X.S. Sulige field in the Ordos Basin: Geological setting, field discovery and tight gas reservoirs. *Mar. Pet. Geol.* **2008**, *25*, 387–400. [CrossRef]
7. Hu, G.Y.; Li, J.; Shan, X.Q.; Han, Z.X. The origin of natural gas and the hydrocarbon charging history of the Yulin gas field in the Ordos Basin, China. *Int. J. Coal Geol.* **2010**, *81*, 381–391.
8. Dai, J.X.; Ni, Y.Y.; Wu, X.Q. Tight gas in China and its significance in exploration and exploitation. *Petrol. Explor. Dev.* **2012**, *39*, 277–284. [CrossRef]
9. Huang, S.P.; Fang XLiu, D.; Fang, C.C.; Huang, T.F. Natural gas genesis and sources in the Zizhou gas field, Ordos Basin, China. *Int. J. Coal Geol.* **2015**, *152*, 132–143. [CrossRef]
10. Wu, X.Q.; Ni, C.H.; Liu, Q.Y.; Liu, G.X.; Zhu, J.H.; Chen, Y.B. Genetic types and source of the Upper Paleozoic tight gas in the Hangjinqi area, northern Ordos Basin, China. *Geofluids* **2017**, *2017*, 4596273. [CrossRef]
11. Zou, C.N.; Yang, Z.; Tao, S.Z.; Yuan, X.J.; Zhu, R.K.; Hou, L.H.; Wu, S.T.; Sun, L.; Zhang, G.S.; Bai, B.; et al. Continuous hydrocarbon accumulation over a large area as a distinguishing characteristic of unconventional petroleum: The Ordos Basin, North-Central China. *Earth Sci. Rev.* **2013**, *126*, 358–369. [CrossRef]
12. Yang, Z.; He, S.; Guo, X.W.; Li, Q.; Chen, Z.Y.; Zhao, Y.C. Formation of low permeability reservoirs and gas accumulation process in the Daniudi gas field, northeast Ordos basin, China. *Mar. Pet. Geol.* **2016**, *70*, 222–236. [CrossRef]
13. Xu, N.N.; Qiu, L.W.; Eriksson, K.A.; Klyukin, Y.L.; Wang, Y.; Yang, Y.Q. Influence of detrital composition on the diagenetic history of tight sandstones with implications for reservoir quality: Examples from the Permian Xiashihezi Formation and Carboniferous Taiyuan Formation, Daniudi gas field, Ordos Basin, China. *Mar. Pet. Geol.* **2017**, *88*, 756–784. [CrossRef]
14. Lai, F.P.; Li, Z.P.; Zhang, T.T.; Zhou, A.Q.; Gong, B. Characteristics of microscopic pore structure and its influence on spontaneous imbibition of tight gas reservoir in the Ordos Basin, China. *J. Pet. Sci. Eng.* **2019**, *172*, 23–31. [CrossRef]
15. Huyan, Y.Y.; Pang, X.Q.; Jiang, F.J.; Li, L.L.; Zheng, D.Y.; Shao, X.H. Coupling relationship between tight sandstone reservoir and gas charging: An example from lower Permian Taiyuan Formation in Kangning field, northeastern Ordos Basin, China. *Mar. Pet. Geol.* **2019**, *105*, 238–250. [CrossRef]
16. Zhao, J.; Li, J.; Cao, Q.; Bai, Y.; Wu, W.; Ma, Y. Quasi-continuous hydrocarbon accumulation: An alternative model for the formation of large tight oil and gas accumulations. *J. Pet. Sci. Eng.* **2019**, *174*, 25–39. [CrossRef]
17. Zheng, D.Y.; Pang, X.Q.; Jiang, F.J.; Liu, T.S.; Shao, X.H.; Huyan, Y.Y. Characteristics and controlling factors of tight sandstone gas reservoirs in the Upper Paleozoic strata of Linxing area in the Ordos Basin, China. *J. Nat. Gas Sci. Eng.* **2020**, *75*, 103135. [CrossRef]
18. Wang, R.; Shi, W.Z.; Xie, X.Y.; Zhang, W.; Qin, S.; Liu, K.; Busbey Arthur, B. Clay mineral content, type, and their effects on pore throat structure and reservoir properties: Insight from the Permian tight sandstones in the Hangjinqi area, north Ordos Basin, China. *Mar. Pet. Geol.* **2020**, *115*, 104281. [CrossRef]
19. Qin, S.; Wang, R.; Shi, W.Z.; Liu, K.; Zhang, W.; Xu, X.F.; Qi, R.; Yi, Z.X. Diverse effects of intragranular fractures on reservoir properties, diagenesis, and gas migration: Insight from Permian tight sandstone in the Hangjinqi area, north Ordos Basin. *Mar. Pet. Geol.* **2022**, *137*, 105526. [CrossRef]
20. Bai, D.L.; Yang, M.H.; Lei, Z.B.; Zhang, Y. Effect of tectonic evolution on hydrocarbon charging time: A case study from Lower Shihezi Formation (Guadalupian), the Hangjinqi area, northern Ordos, China. *J. Pet. Sci. Eng.* **2020**, *184*, 106465. [CrossRef]
21. Liu, K.; Wang, R.; Shi, W.Z.; Zhang, W.; Qi, R.; Qin, S.; Xu, L.T. Tectonic controls on Permian tight gas accumulation: Constrains from fluid inclusion and paleo-structure reconstruction in the Hangjinqi area, northern Ordos Basin, China. *J. Nat. Gas Sci. Eng.* **2020**, *86*, 103616. [CrossRef]
22. Xiao, X.M.; Zhao, B.Q.; Thu, Z.L.; Song, Z.G.; Wilkins, R.W.T. Upper Paleozoic petroleum system, Ordos Basin, China. *Mar. Pet. Geol.* **2005**, *22*, 945–963. [CrossRef]
23. Xie, X.Y.; Heller, P.L. U-Pb detrital zircon geochronology and its implications: The early Late Triassic Yanchang Formation, south Ordos Basin, China. *J. Asian Earth Sci.* **2013**, *64*, 86–98. [CrossRef]
24. Yang, M.H.; Li, L.; Zhou, J.; Jia, H.C.; Sun, X.; Qu, X.Y.; Zhou, D.; Gong, T.; Ding, C. Mesozoic structural evolution of the Hangjinqi area in the northern Ordos Basin, North China. *Mar. Pet. Geol.* **2015**, *66*, 695–710. [CrossRef]
25. Hanson, A.D.; Ritts, B.D.; Moldowan, J.M. Organic Geochemistry of oil and source rock strata of the Ordos Basin, north-central China. *AAPG Bull.* **2007**, *91*, 1273–1293. [CrossRef]
26. Xu, Q.H.; Shi, W.Z.; Xie, X.Y.; Busbey, A.B.; Xu, L.T.; Wu, R.; Liu, K. Inversion and propagation of the late paleozoic porjianghaizi fault (north Ordos basin, China): Controls on sedimentation and gas accumulations. *Mar. Pet. Geol.* **2018**, *91*, 706–722. [CrossRef]
27. Schaefer, R.G.; GalushkinRitts, B.D.; Hansonb, A.D.; Darbyc, B.J.; Nansona, L.; Berry, A. Sedimentary record of triassic intraplate extension in north China: Evidence from the nonmarine NW Ordos Basin, helan Shan and zhuozi Shan. *Tectonophysics* **2004**, *386*, 177–202.
28. Zhang, Z.; Sun, K.; Yin, J. Sedimentology and sequence stratigraphy of the P1s (Lower Permian) in the northwestern Ordos Basin, China: An alternative sequence model for fluvial strata. *Sediment. Geol.* **1997**, *112*, 123–136. [CrossRef]
29. Zhu, H.; Chen, K.; Liu, K.; Hel, S. A sequence stratigraphic model for reservoir sand-body distribution in the Lower Permian Shanxi Formation in the Ordos Basin, northern China. *Mar. Pet. Geol.* **2008**, *25*, 731–743. [CrossRef]

30. Li, Y.; Gao, X.; Meng, S.; Wu, P.; Niu, X.; Qiao, P.; Derek, E. Diagenetic sequences of continuously deposited tight sandstones in various environments: A case study from upper Paleozoic sandstones in the Linxing area, eastern Ordos basin, China. *AAPG Bull.* **2019**, *103*, 2757–2783. [CrossRef]

31. Anees, A.; Shi, W.Z.; Ashraf, U.; Xu, Q.H. Channel identification using 3D seismic attributes and well logging in lower Shihezi Formation of Hangjinqi area, northern Ordos Basin, China. *J. Appl. Geophys.* **2019**, *163*, 139–150. [CrossRef]

32. Zhao, J.Z.; Zhang, W.Z.; Li, J.; Cao, Q.; Fan, Y.F. Genesis of tight sand gas in the Ordos Basin, China. *Org. Geochem.* **2014**, *74*, 76–84. [CrossRef]

33. Beard, D.C.; Weyl, P.K. Influence of texture on porosity and permeability of unconsolidated sand. *AAPG Bull.* **1973**, *57*, 349–369.

34. Ping, H.; Chen, H.; Thiéry, R. Thermodynamic modeling of petroleum inclusions: Composition modeling and prediction of the trapping pressure of crude oils. *Fluid Phase Equilib.* **2013**, *346*, 33–44. [CrossRef]

35. Ping, H.; Chen, H.; Jia, G. Petroleum accumulation in the deeply buried reservoirs in the northern Dongying Depression, Bohai Bay Basin, China: New insights from fluid inclusions, natural gas geochemistry, and 1-d basin modeling. *Mar. Pet. Geol.* **2017**, *80*, 70–93. [CrossRef]

36. Chen, R.; Luo, X.; Chen, Z.; Yu, J.; Yang, Y. Restoration of burial history of four periods in Ordos Basin. *Acta Pet. Sin.* **2006**, *27*, 43–47, (In Chinese with English Abstract).

37. Ren, Z.L.; Yu, Q.; Cui, J.P.; Qi, K.; Chen, Z.J.; Cao, Z.P.; Yang, P. Thermal history and its controls on oil and gas of the Ordos Basin. *Earth Sci. Front.* **2017**, *24*, 137–148, (In Chinese with English Abstract).

38. Wygrala, B.P. Integrated Study of an Oil Field in the Southern Po Basin, Northern Italy. Ph.D. Thesis, Berichte des Forschungszentrums Juelich, Jülich, Germany, 1989; p. 217.

39. Sweeney, J.J.; Burnham, A.K. Evaluation of a Simple Model of Vitrinite Reflectance Based on Chemical Kinetics. *AAPG Bull.* **1990**, *74*, 1559–1570.

40. Xue, H.; Zhang, J.C.; Xu, B.; Wang, Y.; Mao, X.P. Evaluation of Upper Paleozoic source rocks of the Hangjinqi block in the northern Ordos basin, China. *J. Chengdu Univ. Technol.* **2010**, *37*, 21–28, (In Chinese with English Abstract).

41. Liu, J.L.; Liu, K.Y.; Huang, X. Effect of sedimentary heterogeneities on hydrocarbon accumulations in the Permian Shanxi Formation, Ordos Basin, China: Insight from an integrated stratigraphic forward and petroleum system modelling. *Mar. Pet. Geol.* **2016**, *76*, 412–431. [CrossRef]

42. Bjørlykke, K.; Aagaard, P. Clay Minerals in North Sea Sandstones. In *Origin, Diagenesis and Petrophysics of Clay Minerals in Sandstones 47*; Houseknecht, D.W., Pittman, E.D., Eds.; SEPM Special Publication: Tulsa, OK, USA, 1992; pp. 65–80.

43. Hagemann, H.W.; Hollerbach, A. The fluorescence behaviour of crude oils with respect to their thermal maturation and degradation. *Org. Geochem.* **1986**, *10*, 473–480. [CrossRef]

44. Du, X.; Zheng, H.Y.; Jiao, X.Q. Abnormal pressure and hydrocarbon accumulation. *Earth Sci. Front.* **1995**, *4*, 137–148, (In Chinese with English Abstract).

45. *SY/T 5477*; Petroleum and Gas Industry Standard, People's Republic of China. State of Economic and Trade Commission: Beijing, China, 2003. (In Chinese)

46. Wang, Y.; Liu, L.F.; Li, S.T.; Ji, H.T.; Xu, Z.J.; Luo, Z.H.; Xu, T.; Li, L.Z. The forming mechanism and process of tight oil sand reservoirs: A case study of Chang 8 oil layers of the Upper Triassic Yanchang Formation in the western Jiyuan area of the Ordos Basin, China. *J. Pet. Sci. Eng.* **2017**, *158*, 29–46. [CrossRef]

47. Henares, S.; Caracciolo, L.; Viseras, C.; Fernandez, J.; Yeste, L.M. Diagenetic constraints on heterogeneous reservoir quality assessment: A Triassic outcrop analog of meandering fluvial reservoirs. *AAPG Bull.* **2016**, *100*, 1377–1398. [CrossRef]

48. Lai, J.; Wang, G.W.; Wang, S.; Cao, J.T.; Li, M.; Pang, X.J.; Zhou, Z.L.; Fan, X.Q.; Dai, Q.Q.; Yang, L.; et al. Review of diagenetic facies in tight sandstones: Diagenesis, diagenetic minerals, and prediction via well logs. *Earth Sci. Rev.* **2018**, *185*, 234–258. [CrossRef]

49. Bjørlykke, K.; Jahren, J. Open or closed geochemical systems during diagenesis in sedimentary basins: Constraints on mass transfer during diagenesis and the prediction of porosity in sandstone and carbonate reservoirs. *AAPG Bull.* **2012**, *96*, 2193–2214. [CrossRef]

50. Cao, B.; Luo, X.; Zhang, L.; Sui, F.; Lin, H.; Lei, Y. Diagenetic evolution of deep sandstones and multiple-stage oil entrapment: A case study from the Lower Jurassic Sangonghe Formation in the Fukang Sag, Central Junggar basin (NW China). *J. Pet. Sci. Eng.* **2017**, *152*, 136–155. [CrossRef]

51. Qiu, L.W.; Mu, X.J.; Li, H.; Zhang, J.; Ge, J.; Xu, S.; Zhou, S.B. Characteristics of detritus development in the Permian lower Shihezi Formation in Hangjinqi area and its influence on reservoir physical properties. *Oil Gas Geol.* **2019**, *40*, 24–33, (In Chinese with English Abstract).

52. Mansurbeg, H.; Morad, S.; Salem, A.; Marfil, R.; El-Ghali, M.A.K.; Nystuen, J.P.; Caja, M.A.; Amorosi, A.; Garcia, G.; Iglesia, A.L. Diagenesis and reservoir quality evolution of palaeocene deep-water, marine sandstones, the Shetland-Faroes Basin, British continental shelf. *Mar. Pet. Geol.* **2008**, *25*, 514–543. [CrossRef]

53. Swarbrick, R.E.; Osborne, M.J.; Yardley, G.S. Comparison of overpressure magnitude resulting from the main generating mechanisms. In *Pressure Regimes in Sedimentary Basins and Their Prediction*; Huffman, A.R., Bowers, G.L., Eds.; AAPG Memoir: Tulsa, OK, USA, 2002; Volume 76, pp. 1–12.

54. Zhao, J.Z.; Li, J.; Xu, Z.Y. Advances in the origin of overpressures in sedimentary basins. *Acta Pet. Sin.* **2017**, *38*, 973–998, (In Chinese with English Abstract). [CrossRef]

55. Li, J.; Zhao, J.Z.; Wei, X.S.; Chen, M.N.; Song, P.; Han, Z.H.; Wu, W.T. Origin of abnormal pressure in the Upper Paleozoic shale of the Ordos Basin, China. *Mar. Pet. Geol.* **2019**, *110*, 162–177. [CrossRef]

56. Osborne, M.J.; Swarbrick, R.E. Mechanisms for generating overpressure in sedimentary basins: A reevaluation. *AAPG Bull.* **1997**, *81*, 1023–1041.

57. Wang, X.; He, S.; Wei, A.J.; Liu, Q.; Liu, C.H. Typical disequilibrium compaction caused overpressure of Paleocene Dongying Formation in northwest Liaodongwan Depression, Bohai Bay Basin, China. *J. Pet. Sci. Eng.* **2016**, *147*, 726–734. [CrossRef]

58. Su, A.; Chen, H.H.; Lei, M.Z.; Li, Q.; Wang, C.W. Paleo-pressure evolution and its origin in the Pinghu slope belt of the Xihu Depression, East China Sea Basin. *Mar. Pet. Geol.* **2019**, *107*, 98–213. [CrossRef]

59. Horsfield, B.; Schenk, H.J.; Mills, N.; Welte, D.H. An investigation of the in-reservoir conversion of oil to gas: Compositional and kinetic findings from closed-system programmed-temperature pyrolysis. *Org. Geochem.* **1992**, *19*, 191–204. [CrossRef]

60. Luo, X.; Vasseur, G. Contributions of compaction and aquathermal pressuring to geopressure and the influence of environmental conditions. *AAPG Bull.* **1992**, *76*, 1550–1559.

61. Wang, W.L.; Zhang, Y.M.; Zhao, J. Evolution of formation pressure and accumulation of natural gas in the Upper Palaeozoic, eastern-central Ordos Basin, Central China. *Geol. J.* **2018**, *53* (Suppl. S2), 395–404. [CrossRef]

62. Xia, L.; Liu, Z.; Cao, Y.C.; Zhang, W.; Liu, J.B.; Yu, C.L.; Hou, Y.J. Postaccumulation sandstone porosity evolution by mechanical compaction and the effect on gas saturation: Case study of the Lower Shihezi Formation in the Bayan'aobao area, Ordos Basin, China. *Mar. Pet. Geol.* **2020**, *115*, 104253. [CrossRef]

63. Duan, Y.; Wu, Y.Z. Distribution and formation of Mesozoic low permeability underpressured oil reservoirs in the Ordos Basin, China. *J. Pet. Sci. Eng.* **2020**, *187*, 106755. [CrossRef]

64. Corbet, T.F.; Bethke, C.M. Disequilibrium fluid pressures and groundwater flow in the Eastern Canada Sedimentary Basin. *J. Geophys. Res.* **1992**, *97*, 7203–7217. [CrossRef]

65. Xia, X.; Song, Y. Temperature effects on geopressure during deposition and erosion. *Petrol. Explor. Dev.* **2001**, *28*, 8–11.

66. Chen, G.; Ding, C.; Xu, L.M.; Zhang, H.R.; Li, N.; Li, Y.; Hu, Y.X.; Huang, D.S. Indirect dating of multi-stage hydrocarbon accumulations by fluid inclusion data: A case study of the Permian hydrocarbon accumulation in the northeast Ordos Basin. *Acta Petrol. Sin.* **2012**, *33*, 1003–1011, (In Chinese with English Abstract).

67. Guo, Y.C.; Pang, X.Q.; Li, Z.X.; Guo, F.T.; Song, L.C. The critical buoyancy threshold for tight sandstone gas entrapment: Physical simulation, interpretation, and implications to the Upper Paleozoic Ordos Basin. *J. Pet. Sci. Eng.* **2017**, *149*, 88–97. [CrossRef]

68. Parnell, J.; Carey, P.F.; Monson, B. Fluid inclusion constraints on temperatures of petroleum migration from authigenic quartz in bitumen veins. *Chem. Geol.* **1996**, *129*, 217–226. [CrossRef]

69. Shu, Y.; Lin, Y.X.; Liu, Y.; Yu, Z.Y. Control of magmatism on gas accumulation in Linxing area, Ordos Basin, NW China: Evidence from fluid inclusions. *J. Pet. Sci. Eng.* **2019**, *180*, 1077–1087. [CrossRef]